Published on 11 June 2021. Downloaded by Australian National University on 10/23/2023 8:57:53 PM.

PCCP

ROYAL SOCIETY OF CHEMISTRY

PAPER

View Article Online
View Journal | View Issue

Cite this: Phys. Chem. Chem. Phys., 2021, 23, 14231

Received 11th May 2021,
Accepted 10th June 2021

DOI: 10.1039/d1cp02063c

rsc.li/pccp

Ion track etching of polycarbonate membranes monitored by *in situ* small angle X-ray scattering†

Alexander Kiy, *[a] Christian Notthoff, [a] Shankar Dutt,[a] Mark Grigg,[a] Andrea Hadley,[a] Pablo Mota-Santiago,[b] Nigel Kirby,[b] Christina Trautmann,[cd] Maria E. Toimil-Molares[d] and Patrick Kluth [a]

In situ small angle X-ray scattering (SAXS) measurements of ion track etching in polycarbonate foils are used to directly monitor the selective dissolution of ion tracks with high precision, including the early stages of etching. Detailed information about the track etching kinetics and size, shape, and size distribution of an ensemble of nanopores is obtained. Time resolved measurements as a function of temperature and etchant concentration show that the pore radius increases almost linearly with time for all conditions and the etching process can be described by an Arrhenius law. The radial etching shows a power law dependency on the etchant concentration. An increase in the etch rate with increasing temperature or concentration of the etchant reduces the penetration of the etchant into the polymer but does not affect the pore size distribution. The *in situ* measurements provide an estimate for the track etch rate, which is found to be approximately three orders of magnitude higher than the radial etch rate. The measurement methodology enables new experiments studying membrane fabrication and performance in liquid environments.

1 Introduction

Membranes containing nano-sized pores have gained relevance in areas such as ultrafiltration, bio- and medical sensing, nanofluidics and nano-electronic devices.[1–6] Nowadays even membranes with only one single nanopore can be manufactured. They are of interest as building blocks for sensors for a variety of analytes such as single ions, single molecules, biochemicals or drugs.[7–11] These applications can greatly benefit from nanoengineered pores with controlled shapes and uniform sizes. Nanopore membranes with extremely narrow pore size distribution and controlled pore density, down to a single pore, can be fabricated using high-energy ion irradiation and subsequent chemical etching, which yields so called 'track-etched membranes'.[12,13] This process is used for the commercial fabrication of nanopore membranes made from various polymers such as polycarbonate, polyethylene terephthalate and polyimide. The pore diameter ranges from a few μm down to ∼20 nm with their length determined by the foil thickness, typically between 10 and 30 μm.[13] Depending on the material and etching conditions, the shape of the etched pores can be cylindrical, (bi)conical or cigar/bullet like.[11,14]

The concept of using high-energy particle tracks and chemical etching for the fabrication of nanopores has first been described by Fleischer *et al.*[15,16] The technique is based on the phenomenon of high-energetic ions/particles leaving straight, very narrow trails of permanent damage in many solids, so called 'ion tracks'. In most materials, the damaged regions are more susceptible to chemical etching than the bulk material. In polymers, the chemical etch rate between damaged and undamaged material differs by several orders of magnitude. Each individual track is thus converted into a long, narrow channel extending through the polymer.

Three different etch rates are commonly employed to describe the chemical etching of a given ion track, the track etch rate V_t, the bulk etch rate V_b, and the radial etch rate V_r. The track etch rate denotes the rate at which the heavily damaged region is dissolved along the ion track. The core of this damaged region has a diameter between 3 and 10 nm, depending on the energy loss of the ion projectile.[5,17,18] The bulk etch rate V_b describes the etch rate of the undamaged matrix and is isotropic for a homogeneous material. The etching process proceeds simultaneously along the track and in the direction perpendicular to the track axis (radial etching). If V_t is significantly higher than V_b, the track is converted into an

[a] Department of Electronic Materials Engineering, Research School of Physics, Australian National University, Canberra ACT 2601, Australia. E-mail: alexander.kiy@anu.edu.au
[b] Australian Synchrotron, ANSTO, 800 Blackburn Rd, Clayton VIC 3168, Australia
[c] GSI Helmholtzzentrum für Schwerionenforschung, Planckstr. 1, 64291 Darmstadt, Germany
[d] Technische Universität Darmstadt, 64289 Darmstadt, Germany

† Electronic supplementary information (ESI) available. See DOI: 10.1039/d1cp02063c

Published on 11 June 2021. Downloaded by Australian National University on 10/23/2023 8:57:53 PM.

open channel. The channel geometry is determined by the ratio of V_t to V_b, which depends on factors such as concentration and temperature of the etchant, and by the energy loss of the ions. Once the track material is dissolved, the channel is open and further grows with the radial etch rate V_r. In the initial etching stage, the radial etch rate can slightly differ from V_b for several reasons including the curved surface of the channel, radiolytic defects in the track halo surrounding the core, or limited supply of etchant into the channel and the presence of etching products. In general, the larger the V_t to V_b ratio, the more cylindrical the nanopore becomes.[14] In vitreous SiO_2, the track etch rate is only slightly higher than the bulk etch rate, resulting in conical pores.[19] In contrast, for polymers the track etch rate is higher by several orders of magnitude and thus the resulting etched tracks resemble almost cylindrical pores.

The concept of track etching has been described in detail, and theoretical models explaining the process have been developed.[5,14] However, discrepancies between modeling and experimental observations can arise, as several parameters influence the track etching process. This includes, but is not limited to, the manufacturing process of the polymer, the etching conditions as well as the irradiation parameters (ion species and energy) and post-irradiation treatment using UV exposure. Aging effects on etching of nanopores in polymers and the influence of exposure to oxygen have also been reported.[20]

In the past, track-etched nanopore membranes were studied by a variety of techniques. Microscopy techniques such as atomic force microscopy or scanning electron microscopy have been used to characterize individual nanopores and provide the dimension and size distribution of the nanopores but the information is limited to the membrane surface.[21,22] Monitoring the pore etching is feasible with conductometric measurements, where the ionic current of an electrolyte across the membrane is measured.[23–25] This allows to determine the time to pore breakthrough, and subsequently the growth of the pores by relating the current to their size. However, there is no direct information about the shape of the channels in the bulk of the membrane. Detailed information is typically obtained for membranes containing one single channel.[26] Furthermore, the electrical potential may affect the pore formation process.[27,28]

Here we present an alternative approach by monitoring the etching process *in situ* using small-angle X-ray scattering (SAXS). As demonstrated previously, SAXS provides a powerful tool to analyze track-etched nanopore membranes.[29–31] SAXS measures the entire pore volume and can provide reliable and accurate statistical information about the shape, size, and size distribution.[32–34] Due to the high number of measured scattering objects ($>10^5$), it yields excellent statistics. The high degree of monodispersity and parallelism of the track-etched nanopores allows precise determination of the pore geometry. The high brilliance inherent to a synchrotron source allows fast *in situ* data acquisition, ideal to resolve kinetic processes. In contrast to *ex situ* measurements, where multiple samples are needed, *in situ* SAXS measurements require only one sample warranting the same experimental condition for a measurement series. The drying process prior to any measurement may cause further uncertainties of *ex situ* measurements. Here, we present novel *in situ* SAXS experiments to accurately describe the nanopore etching process in polycarbonate from the early stages to fully etched tracks, using a custom-built etching cell. We demonstrate that this approach enables the detailed study of the track etching kinetics.

2 Methods

2.1 Ion irradiation

Commercially available polycarbonate ($(C_{16}H_{14}O_3)_n$) foils (Makrofol N, Bayer Material Science AG) with 30 μm thickness and a density of 1.21(1) g cm^{-3} were used for the etching experiments. The polymer foils were irradiated with 2.2 GeV ^{197}Au ions at the Universal Linear Accelerator UNILAC (GSI Helmholtz Centre for Heavy Ion Research Darmstadt, Germany) at a fluence of 10^9 ions cm^{-2}. This fluence is low enough that the maximum pore overlap is 14.2% at a maximum pore size of 100 nm, which is sufficient to yield high quality SAXS data, as interpore effects are minimized.[35,36] According to calculations with the SRIM-2010 code,[37] the energy loss of the Au ions in polycarbonate is approximately 13 keV nm^{-1} and varies by less than 5% throughout the polymer foil. Hence, the ion energy is sufficient to generate nearly uniform cylindrical damage regions along the ion paths.

2.2 Polymer etching

The irradiated polymer foils were etched in aqueous sodium hydroxide (NaOH) solutions (1 to 6 M, 38.3 to 56.2 °C). The etching was conducted in a custom-built etching cell, which enables *in situ* SAXS measurements of the pore evolution during the etching. The etching cell is shown in Fig. 1 and consists of an aluminum housing that contains a thermistor and two ceramic heaters. The thermistor and the heaters are connected to a PID controller to keep the temperature of the housing constant. In the center of the aluminum housing a Teflon cell is located, which consists of two halves. The two halves are separated by two thin Teflon sheets, in between which the irradiated polymer film is sandwiched. The Teflon cells and the sheets contain an aperture of 5 mm diameter for X-ray transmission through the cell (inset of Fig. 1). Each side of the cell is sealed with a 20 μm thick mica window.

Two Teflon tubes are guided through the aluminum housing and into the Teflon cell. During the path through the heated aluminum block, the etchant is pre-heated close to the desired temperature. As the PID controller controls the temperature of the heating block and not of the etchant directly, there is a difference between the regulated temperature of the block and the temperature of the etchant inside the cell. The temperature in the Teflon cell was calibrated prior to the etching experiment by measuring the temperature of the etchant at the sample position. This calibration enables precise knowledge of the temperature within ±0.5 °C during the etching process. In the cell, the etchant flows across the membrane before leaving the etching cell. A constant flow of 1 ml min^{-1} on each

View Article Online

Published on 11 June 2021. Downloaded by Australian National University on 10/23/2023 8:57:53 PM.

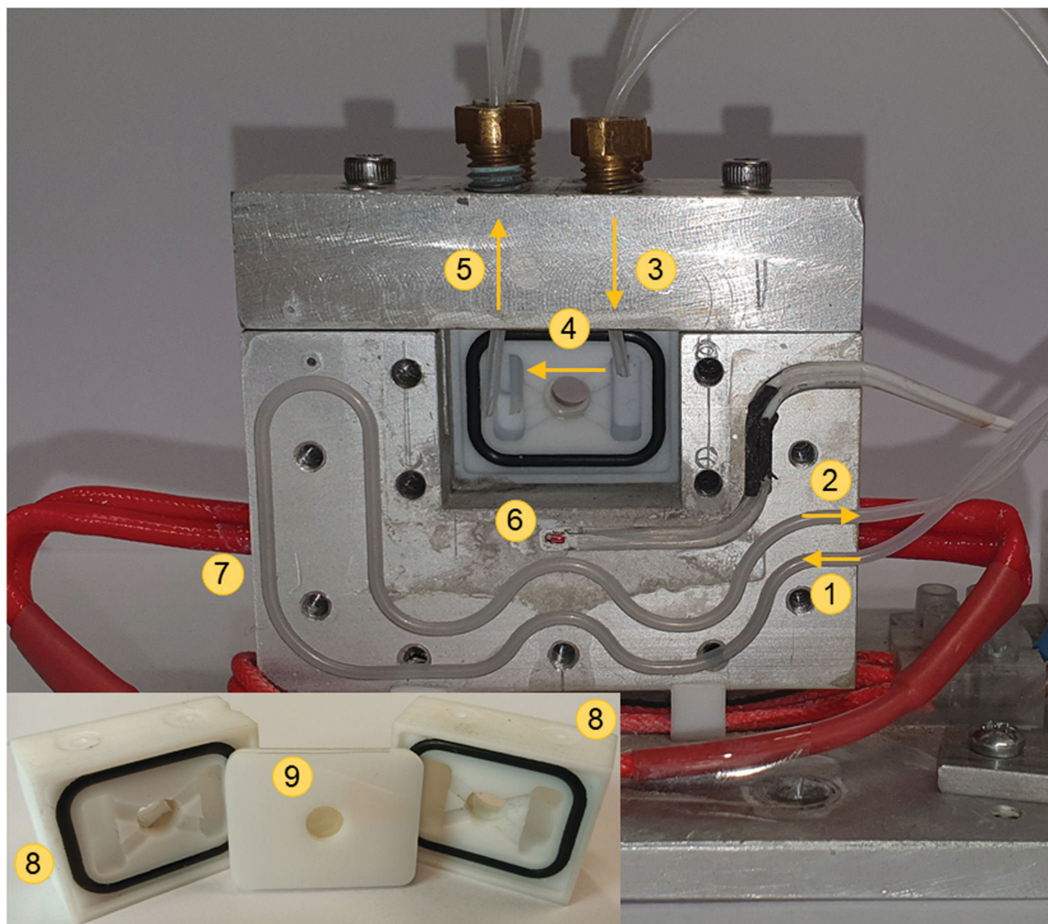

Fig. 1 Custom-built etching cell for *in situ* SAXS measurements. Inset: Teflon cell with a polymer membrane sandwiched in between the Teflon sample holder. ① Cold etchant enters the heating block. ② Heated etchant leaves the heating block. ③ Etchant enters the etching cell. ④ Polymer membrane immersed in etchant with a constant flow past it. ⑤ Etchant exits the etching cell. ⑥ Thermistor. ⑦ Ceramic heaters. ⑧ The two halves of the Teflon cell. ⑨ Polymer membrane sandwiched in between two thin Teflon sheets. The membrane sits in between the two halves of the Teflon cell.

side of the cell is achieved by two individually operating syringe pumps. The flow ensures a constant supply of etchant to prevent etchant depletion and facilitates removal of etching products. The setup also allows etching from one side, with different molarities on each side, and the use of variable flow rates.

Ex situ etching was conducted on a hotplate in a glass beaker with a temperature precision of ±0.2 °C. However, these polycarbonate foils are from a different production and ion irradiation batch, and have a different age compared to the foils used in the *in situ* experiments. *Ex situ* etching was conducted with 3 M NaOH at the same temperatures as the *in situ* experiments between 38.3 and 56.2 °C.

2.3 SAXS measurements

SAXS measurements were carried out at the SAXS/WAXS beamline at the Australian Synchrotron (Melbourne, Australia) with an X-ray energy of 12 keV. Fig. 2 shows the experimental setup at the SAXS/WAXS beamline. The sample cell was mounted on a three-axis goniometer, enabling positioning and tilting the sample with respect to the X-ray beam. The distance between the sample and the Pilatus photon counting detector by Dectris was calibrated using silver behenate ($AgC_{22}H_{43}O_2$) and was approximately 7.2 m. In a typical *in situ* SAXS experiment, the total acquisition time is 6.8 s for each measurement, during which the scattering intensity for the increasing radius is averaged over this time. This is sufficient to yield high quality data and a good time resolution to resolve the track etching process.

The maximum change in pore size during the acquisition of SAXS images is approximately 1 nm and is considered negligible. To verify this, we assumed a constant change of the radius over the acquisition time of 6.8 s. Modeling shown in the ESI,† Fig. S1, shows that this has no significant influence on the data.

2.4 Data acquisition and analysis

Fig. 3 shows typical 2D SAXS patterns of a polycarbonate foil inside the etching cell at different stages of the track etching process. Fig. 3a corresponds to the membrane after swift heavy ion irradiation but prior to etching while mounted in the etching cell. Fig. 3b–d are the 2D SAXS patterns of the irradiated polymer while being immersed in etchant (3 M NaOH, 45.5 °C) at

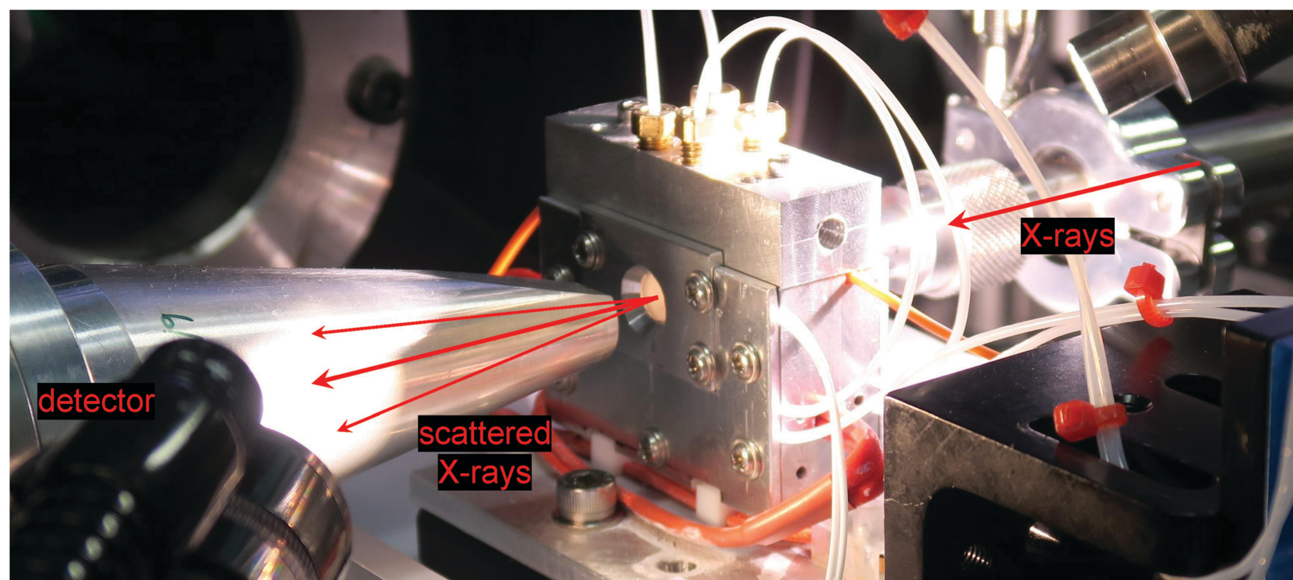

Fig. 2 The experimental setup of *in situ* measurements at the SAXS/WAXS beamline at the Australian Synchrotron. The X-rays exit the vacuum on the right, enter the etching cell and scatter on the sample. The scattered X-rays then re-enter into the vacuum and are detected.

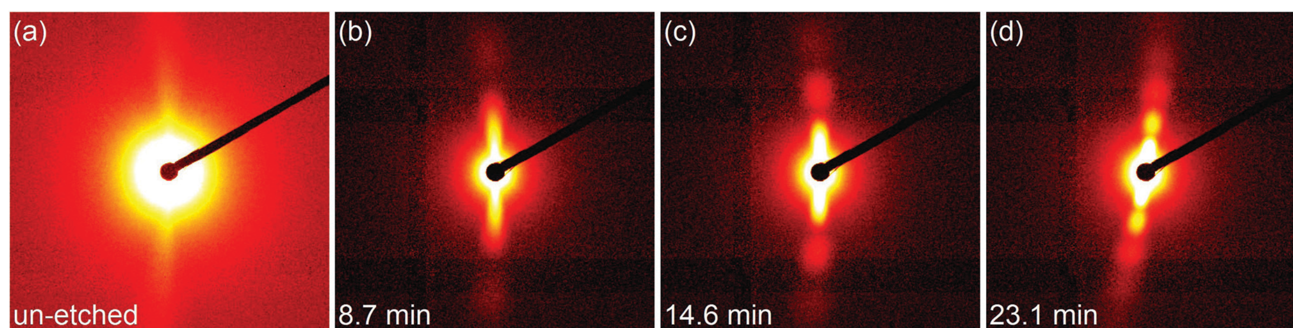

Fig. 3 SAXS detector images inside the etching cell. (a) un-etched and (b–d) during the etching after (b) 8.7 min, (c) 14.6 min and (d) 23.1 min.

Published on 11 June 2021. Downloaded by Australian National University on 10/23/2023 8:57:53 PM.

different stages of the etching process. Due to X-ray absorption of the etchant, the measured scattering intensity is significantly reduced compared to the measurements in air. The images were recorded with the membrane, and accordingly the tracks and pores, tilted by approximately 10° with respect to the X-ray beam. Due to the tilt between the parallel, cylindrical channels and the X-ray beam, the scattering patterns resemble narrow oscillating streaks.[38–40]

To analyze the data, the scattering intensity along the anisotropic streak is extracted and after background subtraction plotted as a 1D scattering intensity as a function of q. q is the magnitude of the scattering vector defined as $q = |\vec{q}| = \frac{4\pi}{\lambda}\sin\theta$, where λ is the wavelength of the incoming X-ray beam and 2θ is the scattering angle as recorded by the detector. The background is obtained by extracting the scattering intensity in an area adjacent to the anisotropic streak.[41,42] The resulting intensity data contains information about the radial density variation of the scattering objects.

Fig. 4 shows the extracted 1D scattering intensities $I(q)$ as a function of the scattering vector q for a polycarbonate membrane from a typical *in situ* experiment. Fig. 4a shows the development of the scattering intensity over time clearly revealing oscillations with maxima that shift towards smaller q with increasing etching time, indicating an increase in the pore radius R. The total scattering intensity increases with etching time as it is proportional to the square of the total scattering volume, *i.e.* $I(q) \propto R^4$. Fig. 4b shows the 1D scattering patterns for selected etching times.

The scattering intensity can be modeled by approximating the nanopores as cylindrical objects with constant electron density difference $\Delta\rho_e$ between the un-etched polymer and the nanopores filled with etchant.[34,43,44] Indicated by the narrow streaks and our prior knowledge about etched tracks in polycarbonate, we assume a cylindrical channel geometry,[32,34] where the cylinder lies on the z-axis of the coordinate system.[45] For a cylindrical object with radius R and length L, the scattering amplitude (form factor) $F(\vec{q},R)$

 This journal is © the Owner Societies 2021

Published on 11 June 2021. Downloaded by Australian National University on 10/23/2023 8:57:53 PM.

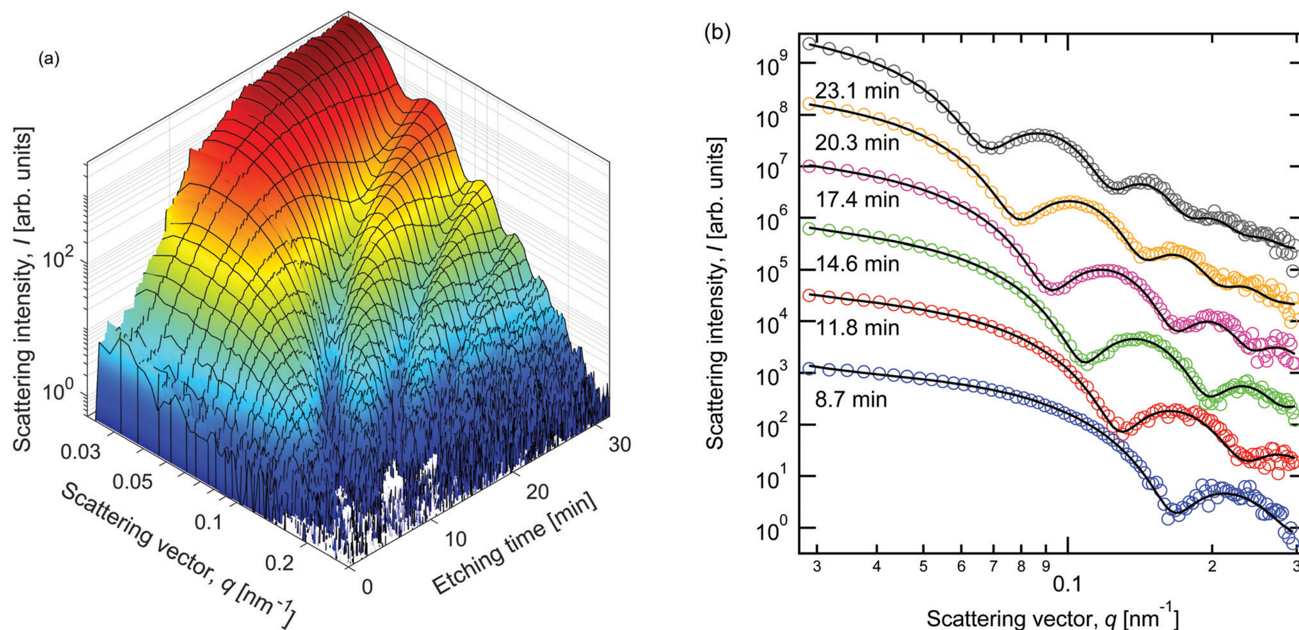

Fig. 4 *In situ* SAXS measurements. (a) Log–log plot of scattering intensities as a function of the scattering vector q and time (linear). (b) Scattering intensities and fits (lines) of etched nanopores recorded for different times during the etching process. Note that the different data sets are offset on the y-axis for better illustration.

along the anisotropic streak ($q_z = 0$) has the form

$$F(\vec{q}, R) = 2\pi R^2 L \Delta\rho_e \frac{\sin\left(q_z \frac{L}{2}\right)}{q_z \frac{L}{2}} \frac{J_1(q_r R)}{q_r R}, \quad (1)$$

where $J_1(q_r R)$ is the Bessel function of the first order.[38] The scattering vector $\vec{q}$ consists of a radial component q_r and a z-component q_z:

$$q_r = |\vec{q}|\cos(\omega) \qquad q_z = |\vec{q}|\sin(\omega). \quad (2)$$

Due to slight bending of the polymer membrane during both ion irradiation and SAXS measurement, the nanopores are not completely parallel. To account for this, a narrow angular distribution with the width Ω (typically $< 0.2°$) around the normal of the surface of the membrane is used to calculate the scattering intensity $I_A(q,R,\Omega)$ of an ensemble of nanopores:

$$I_A(q, R, \Omega) = I_0 \frac{\int_{-\Omega}^{\Omega} |F(\vec{q}, R)|^2 \sin(\omega) d\omega}{\int_{-\Omega}^{\Omega} \sin(\omega) d\omega}, \quad (3)$$

with the forward scattering intensity $I_0 = I(q = 0)$. The angle ω describes the tilt of the nanopores to the normal of the surface of the membrane.

To account for small deviations from perfectly cylindrical, monodisperse pores with a smooth surface, a Gaussian distribution with the standard deviation σ around the mean R is also introduced.[44] The relative standard deviation $\sigma_R = \frac{\sigma}{R}$ describes the standard deviation as a percentage of the radius. This convolution of the intensity considers radial variations between different tracks, *i.e.* the pore size distribution, as well as deviations from a perfect cylinder. The standard deviation also models non-discrete or soft boundaries between the polymer matrix and the etchant during the etching experiments. Depending on the context, we will either refer to the absolute σ or relative σ_R standard deviation (SD).

Two different contributions to the scattering background are considered, a constant background I_b that is a correction to the data at high q at which the background subtraction is inaccurate due to polarization effects that affect the intensity at the edge of the detector, and a q-dependent background I_q that approximates multiple scattering events of the nanopores, which is significant at low q-values.[46] Multiple scattering becomes important when the scatterers' volume becomes large. We observe a relevant contribution of multiple scattering at pore radii above 60 nm.

The total scattering intensity $I(q,R,\Omega,\sigma) = I(q)$ can then be calculated as a function of the scattering vector q:

$$I(q) = I(q, R, \Omega, \sigma) = \frac{\int_0^\infty \exp\left(\frac{-(R-r)^2}{2\sigma^2}\right) I_A(q, R) dR}{\int_0^\infty \exp\left(\frac{-(R-r)^2}{2\sigma^2}\right) dR} + I_b + \frac{I_q}{q^4}. \quad (4)$$

This model was used to perform non-linear least squares fitting of the scattering intensities of cylindrical nanopores typically between q-values of 0.03 and 1 nm^{-1}. The fitted parameters are the forward scattering intensity I_0, the radius R, the standard deviation σ, the angular distribution Ω, and the two background contributions I_b and I_q. Examples of the fits are shown as solid lines in Fig. 4b and they reproduce the data very well.

Published on 11 June 2021. Downloaded by Australian National University on 10/23/2023 8:57:53 PM.

Consecutive scattering patters from the *in situ* experiment only vary slightly from each other as apparent from Fig. 4. This enables the use of a batch fit method, where the data set is fitted with the parameters of the previous fit as the initial parameters. This is essential, as up to 600 SAXS images are acquired in a single *in situ* experiment, depending on the etching conditions. We started the batch fit at the last image, *i.e.* at large radii where the scattering pattern is well defined. The batch fit then moves backwards in time, towards smaller radii. At very small radii (<30 nm), the scattering images were fitted manually.

3 Results and discussion

3.1 Temperature dependence of the nanopore etching process

To determine the temperature dependence of the radial etch rate of the nanopores, polycarbonate foils were etched (3 M NaOH, 38.3, 45.5, 49 and 52.6 °C). Fig. 5a shows the pore radii as a function of the etching time. Nanopores can be observed from the early stages of the etching process with a radius of down to about 10 nm, which is close to the size of the ion track. The experiments were run until the nanopores reached radii of about 100nm. During the entire etching process, the radius increases mostly linearly. From the linear fits (solid lines in Fig. 5a), we deduced the radial etch rates which are listed in Table 1.

As expected, we observe an Arrhenius dependence of the radial etch rates on the temperature (Fig. 5b). From the linear behavior we can deduce an activation energy for the etching process of $E_r = (0.95 \pm 0.05)$ eV.

Some *in situ* measurements were repeated after four months to assess the reproducibility of the experiments (ESI,† Fig. S2). The same polycarbonate foil was etched at 45.5 °C, which showed a radial etch rate of $V_r = (2.07 \pm 0.11)$ nm min^{-1}. This is within the error of the previous measurement under the same conditions. At a temperature of 47.6 °C the radial etch rate increased to $V_r = (2.82 \pm 0.15)$ nm min^{-1}. In Fig. 5b, these two etch rates are added to the Arrhenius plot (Run 2). The values align very well with the previous results and show that the experiments are reproducible. The radial etch rates are of the same order of magnitude as values reported for polycarbonate in the literature.[33,34,47] However, in those experiments, ion irradiation was performed with different ions and at different ion energies, and etched with an etchant of different concentration and at different temperatures, so that a direct comparison is not feasible.

Fig. 6a shows the relative SDs of the nanopores as a function of the pore radius during the *in situ* etching experiments. For pore radii below 40 nm, the SD was fixed for the fits to the scattering data to achieve stable results for the radius. At pore radii above 60 nm, multiple scattering events have a significant influence on the fitted SD. Multiple scattering was accounted for by including a q-dependent background in the fit. Hence, we calculated the average relative SD of the nanopores only for pore radii between 40 and 60 nm (Fig. 6b and Table 1). As the relative SD is approximately constant in the size range during etching, the SD increases at the same rate as the radius. At 52.6 °C, we accidentally etched two polymer foils that were tightly stuck together. This caused two slightly overlapping streaks to appear in the 2D SAXS detector image, one from each foil. We expect the radius values and hence the etch rate to not be influenced by this. However, we cannot reliably deduce the SD from this measurement and hence it is not shown here.

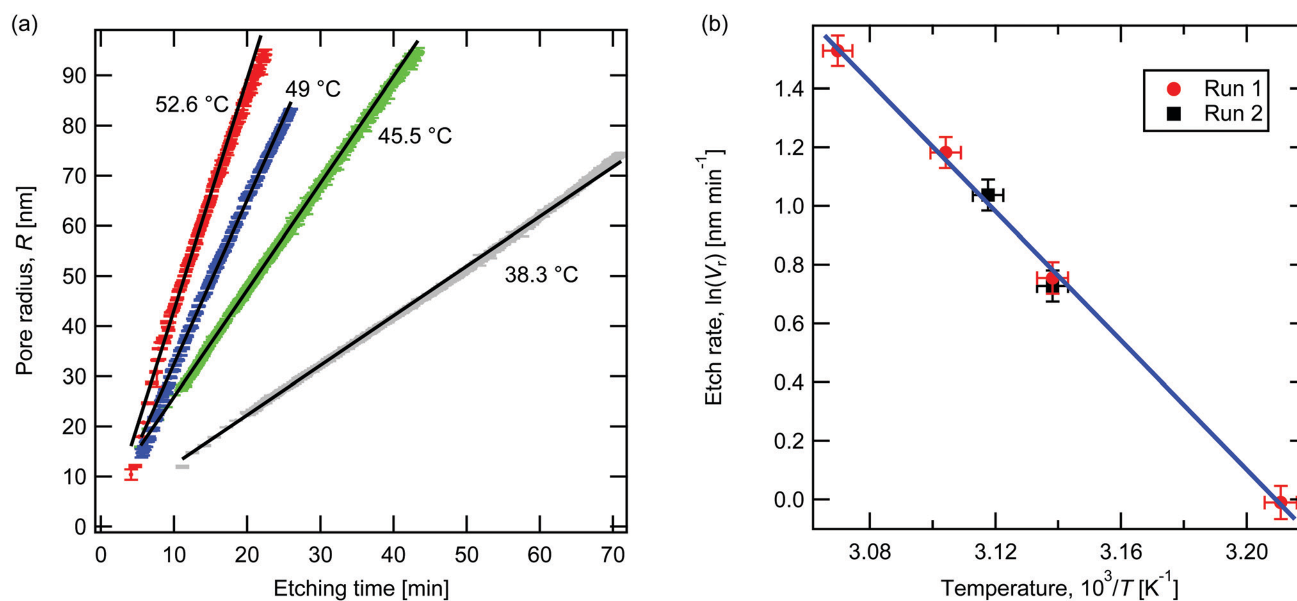

Fig. 5 (a) Pore radii of nanopores as a function of time during etching at 38.3 °C (grey), 45.5 °C (green), 49 °C (blue) and 52.6 °C (red). (b) Arrhenius plot of the radial etch rates deduced from (a) (red circles) and corresponding fit (blue line). The black squares show results from a different run at 45.5 °C and 47.6 °C (ESI,† Fig. S2).

 This journal is © the Owner Societies 2021

Table 1 Radial etch rates V_r and relative SDs σ_R at different temperatures T

Temperature, T [°C]	38.3	45.5	49	52.6
Etch rate, V_r [nm min^{-1}]	0.99 ± 0.06	2.13 ± 0.12	3.26 ± 0.17	4.61 ± 0.24
Relative SD, σ_R [%]	11.3 ± 1.3	9.9 ± 1.1	7.4 ± 1.1	—

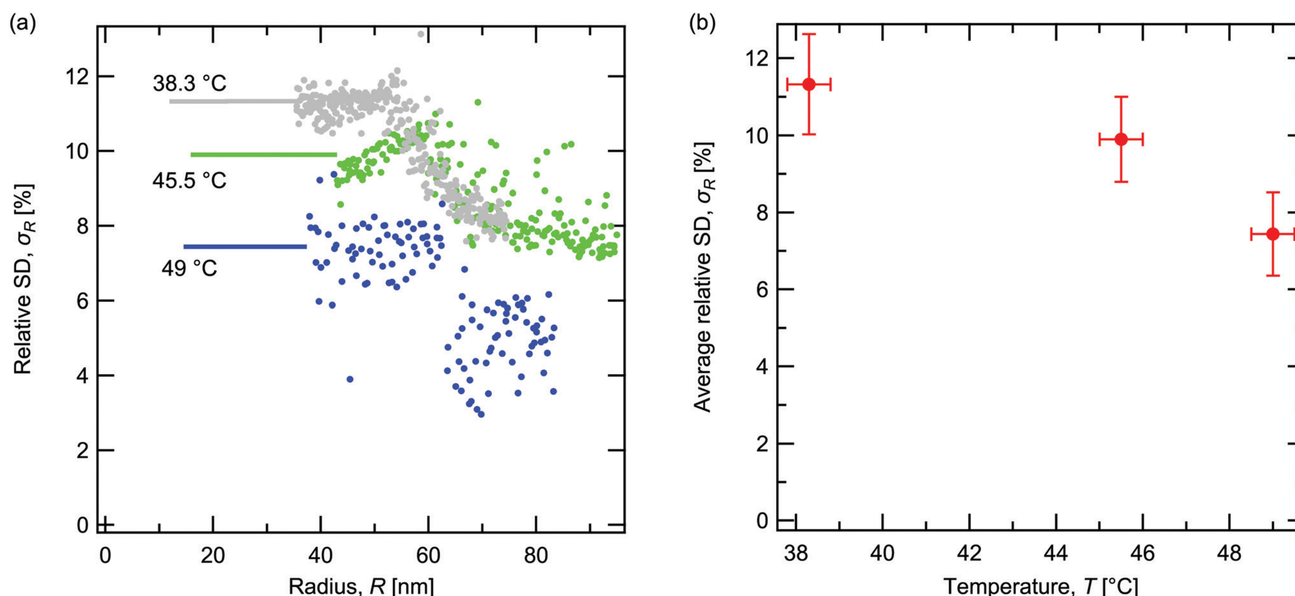

Fig. 6 (a) Relative SDs of nanopores as a function of pore radius during etching at 38.3 °C (grey), 45.5 °C (green) and 49 °C (blue). (b) Average relative SDs of the nanopores with radii between 40 and 60 nm as a function of temperature T.

From Fig. 6 it is apparent that the relative SD decreases with increasing temperature in the *in situ* experiments. The question is if this change in relative SD can be attributed to the differences in homogeneity of the nanopore size distribution or is related to the etching process. To answer this question, we conducted *ex situ* etching experiments, in which we etched polycarbonate foils in a beaker on a hot plate. The foils were etched with the same concentration NaOH at the same temperatures as in the *in situ* experiment (and at 50 °C). For each temperature, three to four membranes were etched to pore sizes between 20 and 150 nm.

After the *ex situ* samples were cleaned with water and dried, all samples showed a similar SD of σ = (3.8 ± 0.9) nm, independent of pore size or temperature (ESI,† Fig. S4 and Table S1). We then immersed those samples in water, and the SD remained unchanged from the dried state. Three observations were made: (i) the SD is different during etching than in the dry state, but the same when being immersed in water and in the dry state. This effect can be attributed to the etching process, and is independent of the liquid. (ii) The SD in the dry/water state is independent of the etching conditions (ESI,† Fig. S5). (iii) The relative SD during etching decreases with increasing temperature.

We conclude that the SD in the dry/water state to be strongly related to the size distribution of the nanopores, as any surface effects on the pore walls would change between being dry and immersed in water. It also indicates that the size variations are not related to the etching conditions, but most likely to the polymer properties and ion irradiation conditions. However, during etching, the relative SD changes with temperature, which indicates that this effect is related to the etching process itself. We associate the relative SD observed during the *in situ* experiments not only with a narrow distribution of the pore radii, but also with the penetration of etchant into the polymer. Fink *et al.* showed that etchant penetrates into the pore walls due to nanocapillary forces.[48,49] This causes swelling of the pores, and the formation of a gel layer at the liquid-polymer interface. In the SAXS measurements, this effect can manifest itself as an increased SD. Fink *et al.* were also able to show that during the initial exposure to the etchant, the amount of absorbed liquid increases rapidly. As etching at higher temperatures is faster, the surface layer is removed at a higher rate and less net penetration occurs compared to lower temperatures. This could result in a lower SD at higher temperatures as observed in our *in situ* SAXS measurements.

From the etching time and the pore radius of the *ex situ* samples, the etch rates were calculated (ESI,† Fig. S3 and Table S1). Interestingly, the *ex situ* etch rates are higher, but the activation energy is E_r = (0.89 ± 0.04) eV, the same (within the uncertainty) as the activation energy obtained by the *in situ* experiments. We can safely rule out temperature as a cause, as both experiments were conducted under well controlled conditions. This indicates that the difference in etching might be caused by the

Published on 11 June 2021. Downloaded by Australian National University on 10/23/2023 8:57:53 PM.

View Article Online

Published on 11 June 2021. Downloaded by Australian National University on 10/23/2023 8:57:53 PM.

different etching setup, and hence the transport of etchant to the pores, as well as the removal of etching products from the pores. To confirm this assumption, we have conducted etching (3 M NaOH, 50 °C) in a beaker on a hotplate, and inside the etching cell with a constant flow of etchant of 1 ml min^{-1} per side, and without flow (ESI,† Fig. S6). We observe radial etch rates of 7.0. 4.9 and 3.9 nm min^{-1}, respectively. This indeed confirms the assumption that in an open space like a beaker transport of etchant and etching products is enhanced compared to etching in a confined space like the etching cell, and using a constant flow promotes the transport compared to stationary etching. These results indicate that the etching setup can have a significant influence on the etching process.

3.2 Concentration dependence of the track etching process

To investigate the relationship between the molarity of the etchant and the radial etch rates, polycarbonate foils were etched (1, 3 and 6 M NaOH, 45.5 °C). The pore radii as a function of the etching time are shown in Fig. 7a. The etching at 6 M is limited to an etching time above 10 min (corresponding to pore radii above 100 nm), as an air bubble on the membrane blocked the etching and we had to move the X-ray beam to a different sample position. The radial etch rates and relative SDs are listed in Table 2.

In Fig. 7b, log(V_r) is plotted against log(c). This shows a power law dependence of the etch rate on the etchant molarity that can be described by

$$V_r = ac^n, \quad (5)$$

where a is a constant and n is the exponent of the power law. In a log–log plot, this monomial appears as a straight line where the slope n equals the exponent of the power law. The linear fit results in an exponent of the power law of $n = 1.38 \pm 0.09$. Fig. 8 shows the relative SD of the nanopores during the etching experiment. It is apparent that an increase in etchant molarity reduces the relative SD of the nanopores. This observation is consistent with the assumption in the last section that the relative SD during the etching is related to the etchant penetration into the polymer. Similar to the temperature effect, a higher molarity, *i.e.* a higher etch rate reduces the amount of absorbed liquid in the track and hence the observed relative SD.

Table 2 Radial etch rates V_r and relative SDs σ_R at different molarities c

Molarity, c [M]	1	3	6
Etch rate, V_r [nm min^{-1}]	0.70 ± 0.01	2.82 ± 0.01	8.46 ± 0.02
Relative SD, σ_R [%]	15.7 ± 4.7	11.5 ± 2.1	4.4 ± 1.3

When comparing the etching of polycarbonate under the same conditions (see Fig. 5a and 7a) in the temperature series and the molarity series (45.5 °C and 3 M), the radial etch rates differ by around 30%. These two etching experiments were conducted with polymer foils that were from different production and ion irradiation batches. This highlights that other factors, such as the polymer membrane and aging of the polymer can have a significant influence on the etching process. We note that using samples from the same batch (as outlined in the previous section) yields reproducible results with our technique.

3.3 Axial track etching

In situ SAXS measurements enable us to estimate the track etch rate V_t at the beginning of the etching process. For the analysis we applied the Guinier approximation for the scattering intensity at small scattering vectors:[50]

$$\lim_{q\to 0} I(q) = I_0 \exp\left(-\frac{1}{3}R_g{}^2q^2\right) + I_b, \quad (6)$$

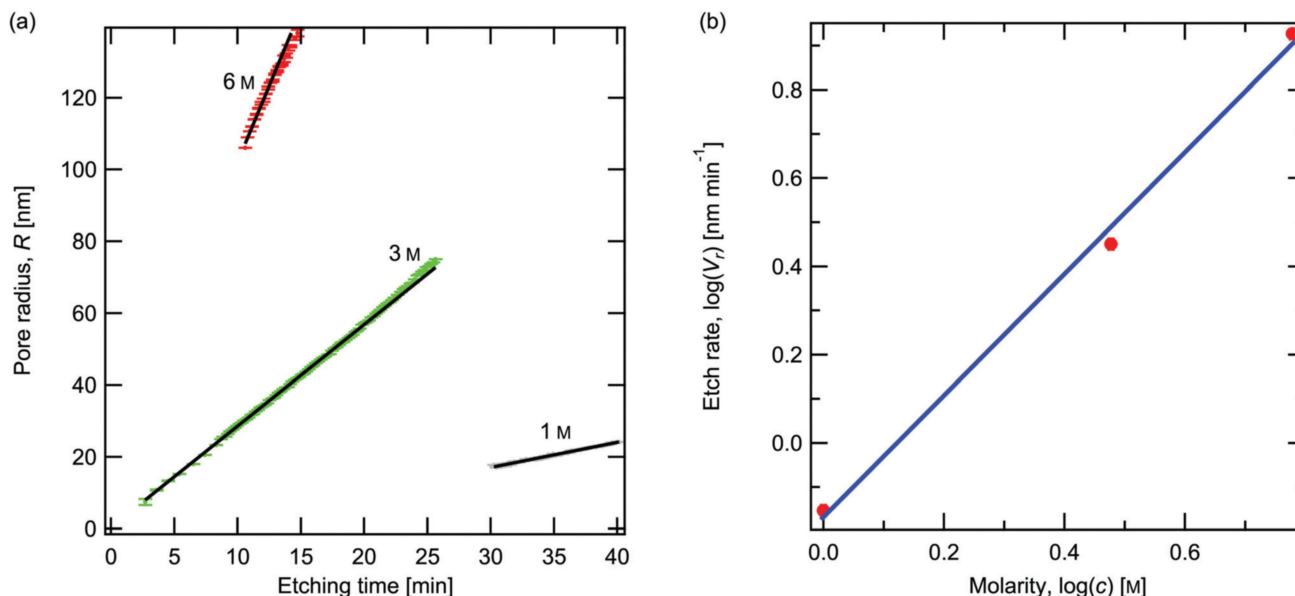

Fig. 7 (a) Pore radii of nanopores as a function of time during etching with 1 M (grey), 3 M (green) and 6 M (red) NaOH. (b) Log–log plot of the radial etch rates as a function of etchant molarity.

This journal is © the Owner Societies 2021

Published on 11 June 2021. Downloaded by Australian National University on 10/23/2023 8:57:53 PM.

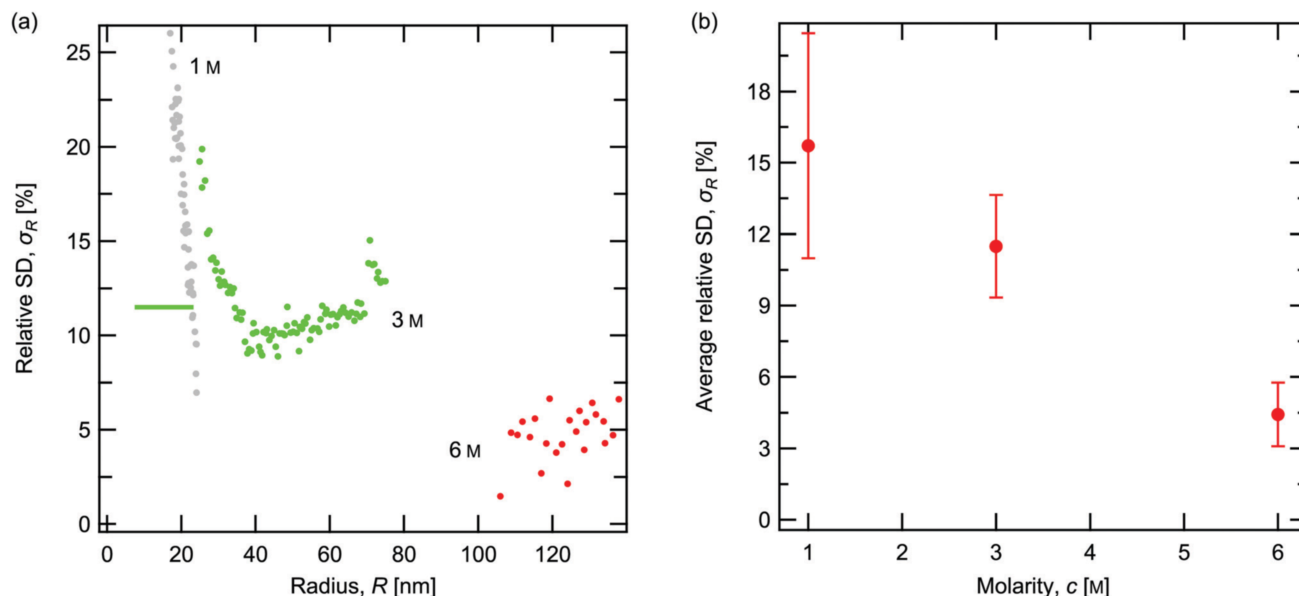

Fig. 8 (a) Relative SDs of nanopores as a function of the pore radius during etching with 1 M (grey), 3 M (green) and 6 M (red) NaOH. (b) Average relative SDs of the nanopores as a function of etchant molarity.

with the forward scattering intensity I_0, the radius of gyration R_g and a scattering background I_b. The forward scattering intensity is given by the electron density contrast $\Delta\rho_e$ between the nanopore and the polymer matrix and the scattering volume V:

$$I_0 = (\Delta\rho_e)^2V^2. \quad (7)$$

Fig. 9a shows the Guinier plot of an example fit for the one-sided *in situ* etching (3 M NaOH and H_2O, 45.5 °C) of the polycarbonate sample after just 80 s of etching, *i.e.* before the pores were etched through. For small values of the scattering vector q, the Guinier approximation describes the scattering pattern very well.

Fig. 9b shows the time development of the forward scattering intensity I_0 that is obtained using the Guinier approximation *versus* time for one-sided and double-sided etching of a polycarbonate foil (3 M NaOH, 45.5 °C, same conditions as in Fig. 4). It is apparent that I_0 is constant or decreases in the first few minutes of etching before it increases rapidly. We attribute this short period to the time dominated by the etching process along

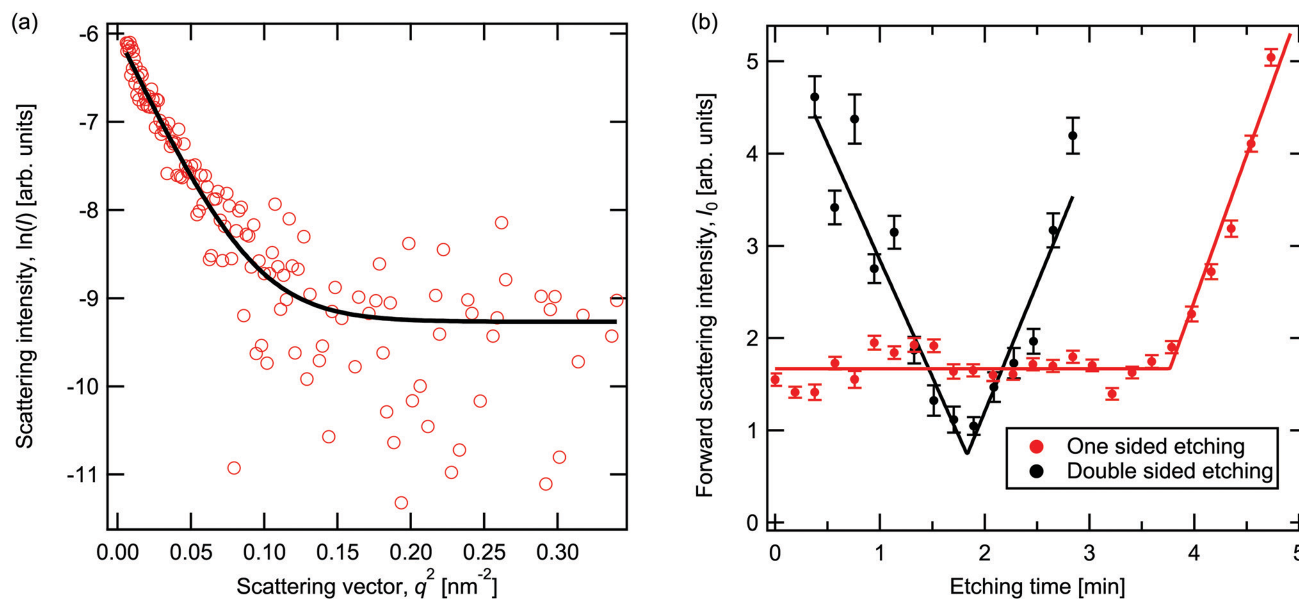

Fig. 9 *In situ* etching to estimate the track etch rate V_t. (a) Guinier plot of the scattering intensity after 80 s of one-sided etching (red). Black line: Guinier approximation of the scattering intensity. (b) Time development of the forward scattering intensity I_0 during the early stages of one-sided etching (red) and of double-sided etching (black).

Published on 11 June 2021. Downloaded by Australian National University on 10/23/2023 8:57:53 PM.

the track axis. During this period, the damaged polymer is dissolved forming an open channel, while radial etching is rather small. Once the track is etched through the polymer film, radial etching speeds up significantly as the transport of etchant is greatly enhanced. This causes a rapid increase in I_0 indicating the breakthrough moment of the channel. With the knowledge of the membrane thickness and the time until I_0 increases rapidly, *i.e.* pore breakthrough, we can estimate the track etch rate.

For one-sided etching, it takes around 3.8 min to etch through. With a membrane thickness of 30 min, this results in a track etch rate of $V_t = (8.0 \pm 0.4)\ \mu m\ min^{-1}$. Etching from both sides takes around 1.8 m, which yields a track etch rate of $V_t = (8.2 \pm 0.9)\ \mu m\ min^{-1}$. The good agreement of the etch rates indicates that this method is viable for determining the track etch rate. The radial etch rate for this specific process is $V_r = (2.13 \pm 0.12)$ nm min^{-1} as reported above, which results in a ratio of $V_t/V_r = 3850 \pm 223$. This aligns well with the value reported by Cornelius *et al.*, who determined a ratio of $V_t/V_r = 2988 \pm 1513$ for Markrofol *N* irradiated with 2.7 GeV U ions and etched with 6 M NaOH at 50 °C.[47] As the track etch rate is higher by three orders of magnitude than the radial etch rate, it also confirms the assumption that the nanopores are nearly cylindrical. This demonstrates that this method can be applied to accurately investigate V_t, which can be the focus of future research.

4 Conclusion

We present novel *in situ* SAXS experiments of ion track etching in polycarbonate. Our measurement technique enables time resolved observation of the growth of nanopores. The measurements were performed under various etching conditions and deliver accurate and detailed results of the etching process of nanopores in polymers. The initial stage of the etching, which is characterized by rapid etching of the highly damaged track core along the ion trajectory, is described by the Guinier approximation. This enables the determination of the track etch rate with higher accuracy than previous methods.

Following pore breakthrough, SAXS patterns were fitted using a simple cylinder model, which assumes a constant electron density difference between a cylindrical pore and the host matrix. This provides accurate information such as the pore radius and standard deviation and their time development during etching. The radial etching was largely linear over time and showed a high sensitivity to the etching conditions. Etching was performed as a function of temperature, which allowed us to deduce the activation energy of the etching processes. The radial etch rate as a function of the etchant molarity shows a power law dependence. The relative SD observed *in situ* is attributed to the penetration of etchant into the polymer. With increasing etch rate, *i.e.* increasing etching temperature or molarity, the etchant penetration into the pore surface is reduced due to a shorter penetration time. Thus this effect has less influence on the overall process and the relative SD decreases. This was confirmed using *ex situ* measurements that showed that the etching conditions or a liquid environment do not affect the size distribution of the nanopores.

With future measurements, we will extend our knowledge about the etching kinetics in nanopore membranes. This will allow us to optimize the controlled fabrication of highly monodisperse nanopore membrane systems.

Conflicts of interest

There are no conflicts to declare.

Acknowledgements

This research was undertaken on the SAXS/WAXS beamline at the Australian Synchrotron, part of ANSTO. The authors acknowledge financial support from the Australian Government through the Australian Research Council.

References

1 B. M. Venkatesan and R. Bashir, *Nat. Nanotechnol.*, 2011, **6**, 615.
2 I. Vlassiouk, P. Apel, S. N. Dmitriev, K. Healy and Z. Siwy, *Proc. Natl. Acad. Sci. U. S. A.*, 2009, **106**, 21039.
3 C. Dekker, *Nat. Nanotechnol.*, 2007, **2**, 209.
4 W. Ensinger, M. Ali, S. Nasir, I. Duznovic, C. Trautmann, M. E. Toimil-Molares, G. R. Distefano, B. Laube, M. Bernhard, M. Mikosch-Wersching, H. F. Schlaak and M. El Khoury, *Int. J. Theor. Appl. Nanotechnol.*, 2018, **6**, 21.
5 D. Fink and V. Hnatowicz, in *Transport Processes in Low-Energy Ion-Irradiated Polymers*, ed. D. Fink, Springer, Berlin, Heidelberg, 2004.
6 H. Hanot and E. Ferain, *Nucl. Instrum. Methods Phys. Res., Sect. B*, 2009, **267**, 1019.
7 Q. Liu, K. Xiao, L. Wen, H. Lu, Y. Liu, X.-Y. Kong, G. Xie, Z. Zhang, Z. Bo and L. Jiang, *J. Am. Chem. Soc.*, 2015, **137**, 11976.
8 S. Howorka and Z. Siwy, *Chem. Soc. Rev.*, 2009, **38**, 2360.
9 L. Wen, Z. Sun, C. Han, B. Imene, D. Tian, H. Li and L. Jiang, *Chem. – Eur. J.*, 2013, **19**, 7686.
10 J. Wang, J. Hou, H. Zhang, Y. Tian and L. Jiang, *ACS Appl. Mater. Interfaces*, 2018, **10**, 2033.
11 G. Pérez-Mitta, M. E. Toimil-Molares, C. Trautmann, W. A. Marmisollé and O. Azzaroni, *Adv. Mater.*, 2019, **31**, 1901483.
12 R. Spohr, *Ion Tracks and Microtechnology: Principles and Applications*, Vieweg + Teubner Verlag, Wiesbaden, 1990.
13 C. Trautmann, in *Ion Beams in Nanoscience and Technology*, ed. R. Hellborg, H. J. Whitlow and Y. Zhang, Springer, Berlin, Heidelberg, 2009.
14 P. Apel, *Radiat. Meas.*, 2001, **34**, 559.
15 R. L. Fleischer, P. B. Price and E. M. Symes, *Science*, 1964, **143**, 249.

This journal is © the Owner Societies 2021

Published on 11 June 2021. Downloaded by Australian National University on 10/23/2023 8:57:53 PM.

16 R. L. Fleischer, P. B. Price and R. M. Walker, *Nuclear tracks in solids: principles and applications*, University of California Press, 1975.
17 P. Apel, R. Spohr, C. Trautmann and V. Vutsadakis, *Radiat. Meas.*, 1999, **31**, 51.
18 T. Steckenreiter, E. Balanzat, H. Fuess and C. Trautmann, *Nucl. Instrum. Methods Phys. Res., Sect. B*, 1999, **151**, 161.
19 A. Hadley, C. Notthoff, P. Mota-Santiago, U. H. Hossain, S. Mudie, M. E. Toimil-Molares, C. Trautmann and P. Kluth, *Nucl. Instrum. Methods Phys. Res., Sect. B*, 2018, **435**, 133.
20 D. Fink, G. Muñoz H., A. García, J. Vacik, V. Hnatowicz, A. Kiv and L. Alfonta, *Nucl. Instrum. Methods Phys. Res., Sect. B*, 2018, **420**, 57.
21 B. N. Miles, A. P. Ivanov, K. A. Wilson, F. Doğan, D. Japrung and J. B. Edel, *Chem. Soc. Rev.*, 2013, **42**, 15.
22 G. Pérez-Mitta, W. A. Marmisollé, L. Burr, M. E. Toimil-Molares, C. Trautmann and O. Azzaroni, *Small*, 2018, **14**, 1703144.
23 C. P. Bean, M. V. Doyle and G. Entine, *J. Appl. Phys.*, 1970, **41**, 1454.
24 P. Apel, *Nucl. Tracks Radiat. Meas.*, 1991, **19**, 29.
25 P. Apel, I. V. Blonskaya, O. L. Orelovitch, B. A. Sartowska and R. Spohr, *Nanotechnology*, 2012, **23**, 225503.
26 P. Apel, Y. E. Korchev, Z. Siwy, R. Spohr and M. Yoshida, *Nucl. Instrum. Methods Phys. Res., Sect. B*, 2001, **184**, 337.
27 C. C. Harrell, Z. Siwy and C. R. Martin, *Small*, 2006, **2**, 194.
28 P. Apel, I. V. Blonskaya, N. E. Lizunov, K. Olejniczak, O. L. Orelovitch, M. E. Toimil-Molares and C. Trautmann, *Small*, 2018, **14**, 1703327.
29 A. V. Semenyuk, D. I. Svergun, L. Y. Mogilevsky, V. V. Berezkin, B. V. Mchedlishvili and A. B. Vasilev, *J. Appl. Crystallogr.*, 1991, **24**, 809.
30 E. Ferain and R. Legras, *Nucl. Instrum. Methods Phys. Res., Sect. B*, 1997, **131**, 97.
31 G. Pépy and A. Kuklin, *Nucl. Instrum. Methods Phys. Res., Sect. B*, 2001, **185**, 198.
32 G. Pépy, E. Balanzat, B. Jean, A. Kuklin, N. Sertova and M. Toulemonde, *J. Appl. Crystallogr.*, 2003, **36**, 649.
33 G. Pépy, P. Boesecke, A. Kuklin, E. Manceau, B. Schiedt, Z. Siwy, M. Toulemonde and C. Trautmann, *J. Appl. Crystallogr.*, 2007, **40**, 388.
34 M. Engel, B. Stühn, J. J. Schneider, T. Cornelius and M. Naumann, *Appl. Phys. A: Mater. Sci. Process.*, 2009, **97**, 99.
35 C. Riedel and R. Spohr, *Radiat. Eff.*, 1979, **42**, 69.
36 P. Kluth, C. S. Schnohr, D. J. Sprouster, A. Byrne, D. J. Cookson and M. C. Ridgway, *Nucl. Instrum. Methods Phys. Res., Sect. B*, 2008, **266**, 2994.
37 J. F. Ziegler, M. D. Ziegler and J. P. Biersack, *Nucl. Instrum. Methods Phys. Res., Sect. B*, 2010, **268**, 1818.
38 D. Schauries, M. D. Rodriguez, B. Afra, T. Bierschenk, C. Trautmann, S. Mudie and P. Kluth, *Nucl. Instrum. Methods Phys. Res., Sect. B*, 2015, **365**, 573.
39 U. H. Hossain, M. D. Rodriguez, D. Schauries, A. Hadley, M. Schleberger, C. Trautmann, S. Mudie and P. Kluth, *Nucl. Instrum. Methods Phys. Res., Sect. B*, 2017, **409**, 293.
40 D. Schauries, P. Mota-Santiago, E. P. Gilbert, N. Kirby, C. Trautmann and P. Kluth, *Eur. Polym. J.*, 2018, **108**, 406.
41 P. Mota-Santiago, H. Vazquez, T. Bierschenk, F. Kremer, A. Nadzri, D. Schauries, F. Djurabekova, K. Nordlund, C. Trautmann, S. Mudie, M. C. Ridgway and P. Kluth, *Nanotechnology*, 2018, **29**, 144004.
42 C. Notthoff, Iontrack SAXS Reduction, https://github.com/cnotthoff/CN_Iontrack_SAXS_Reduction, (accessed April 2021).
43 Y. Eyal and S. Abu Saleh, *J. Appl. Crystallogr.*, 2007, **40**, 71.
44 P. Kluth, C. S. Schnohr, O. H. Pakarinen, F. Djurabekova, D. J. Sprouster, R. Giulian, M. C. Ridgway, A. Byrne, C. Trautmann, D. J. Cookson, K. Nordlund and M. Toulemonde, *Phys. Rev. Lett.*, 2008, **101**, 175503.
45 A. Hadley, C. Notthoff, P. Mota-Santiago, S. Dutt, S. Mudie, M. A. Carrillo-Solano, M. E. Toimil-Molares, C. Trautmann and P. Kluth, *Phys. Rev. Mater.*, 2020, **4**, 056003.
46 G. V. Jensen and J. G. Barker, *J. Appl. Crystallogr.*, 2018, **51**, 1455.
47 T. Cornelius, B. Schiedt, D. Severin, G. Pépy, M. Toulemonde, P. Apel, P. Boesecke and C. Trautmann, *Nanotechnology*, 2010, **21**, 155702.
48 D. Fink, K. K. Dwivedi, M. Müller, S. Ghosh, V. Hnatowicz, J. Vacik and J. Červena, *Radiat. Meas.*, 2000, **32**, 307.
49 D. Fink, A. Petrov, M. Müller, T. Asmus, V. Hnatowicz, J. Vacik and J. Cervena, *Surf. Coat. Technol.*, 2002, **158–159**, 228.
50 A. Guinier, *Ann. Phys.*, 1939, **11**, 161.